JPL PUBLICATION 78-81

Radar Observations of a Volcanic Terrain: Askja Caldera, Iceland

D. L. Evans

October 1, 1978

National Aeronautics and
Space Administration

Jet Propulsion Laboratory
California Institute of Technology
Pasadena, California

JPL PUBLICATION 78-81

Radar Observations of a Volcanic Terrain: Askja Caldera, Iceland

D. L. Evans

October 1, 1978

National Aeronautics and
Space Administration

Jet Propulsion Laboratory
California Institute of Technology
Pasadena, California

The research described in this publication was carried out by the Jet Propulsion Laboratory, California Institute of Technology, under NASA Contract No. NAS7-100.

Abstract

Surface roughness spectra of nine radar backscatter units in the Askja Caldera region of Iceland were predicted from computer-enhanced like- and cross-polarized radar images. A field survey of the caldera was then undertaken to check the accuracy of the preliminary analysis. There was good agreement between predicted surface roughness of backscatter units and surface roughness observed in the field. In some cases, variations in surface roughness could be correlated with previously mapped geologic units.

CONTENTS

Figures

Tables

ACKNOWLEDGEMENTS

I would like to thank C. Elachi, S. Williams, B. Stromberg, and especially T. Farr, all of the Jet Propulsion Laboratory, for supplying some of the data used in this study. The ground photographs were taken by M.C. Malin. This report has benefited from reviews by J.B. Adams and R.C. Bostrom of the University of Washington.

SECTION I
INTRODUCTION

Until recently, side-looking airborne radar images have been used in geological investigations in a similar way to aerial photography to extract morphologic and structural information. Although viewing geometry is different from that of conventional aerial photography, many of the same photointerpretation techniques can be used in the interpretation of radar data. Radar images clearly show topography, linear features, fault scarps, and drainage patterns. A second class of information can also be obtained from radar data since the brightness in each resolution cell of the image is related to the surface roughness and dielectric constant of the imaged terrain.

Recent studies in Death Valley by Schaber et al. (1976) and Daily et al. (1978) have demonstrated correlations between radar reflectivity and the lithology of the surface in alluvial deposits. The purpose of this study was to verify current interpretation techniques such as those used in the Death Valley studies and to investigate the extension of these techniques to nonalluvial terrain. This study involved a test of radar image interpretation which included an analysis of computer-enhanced radar images to determine surface roughness and a subsequent field check to evaluate the accuracy of predictions. The Askja Caldera region in north-central Iceland was chosen as a test site because of the diversity of volcanic surface textures and a paucity of vegetation in the area.

A brief review of the geological setting of Askja is presented in Section II. A general discussion of radar image properties is included in Section III. Computer processing techniques used to enhance the radar data are discussed in Section IV. The correlations between the radar imagery and field observations are described in Section V. Conclusions are presented in Section VI. The theoretical basis for radar backscatter studies is discussed in the Appendix.

SECTION II

GEOLOGIC SETTING

Miocene plateau basalts, dated at 16 million years BP, are the oldest rocks in Iceland (Beloussov and Milanovsky, 1977). Between Middle and Late Miocene times, approximately 9 million years ago, volcanic activity occurred in northeastern and west central Iceland. Subsidence of the middle part of Iceland that resulted in a slight downwarping of the plateau basalts probably also occurred about this time. Gradual subsidence of the crust changed to fracturing and block faulting during a third stage of volcanic activity, approximately 3 million years ago. Volcanism was concentrated in southern Iceland in a band approximately 250 km wide. In northern Iceland, volcanic activity occurred in two areas separated by a stable massif. Basalts and palagonitized basaltic glass were deposited during this stage.

The central grabens of the modern rift system of Iceland were formed approximately 700,000 years ago. The median zone dissects Tertiary Plateau basalts from southwest to northeast. In the south, the zone is separated into two segments by an Upper Tertiary-Quaternary anticline (Fig. 1). Approximately one-third of the lava produced on earth during the past 500 years was erupted in the median zone of Iceland (Thorarinsson, 1965).

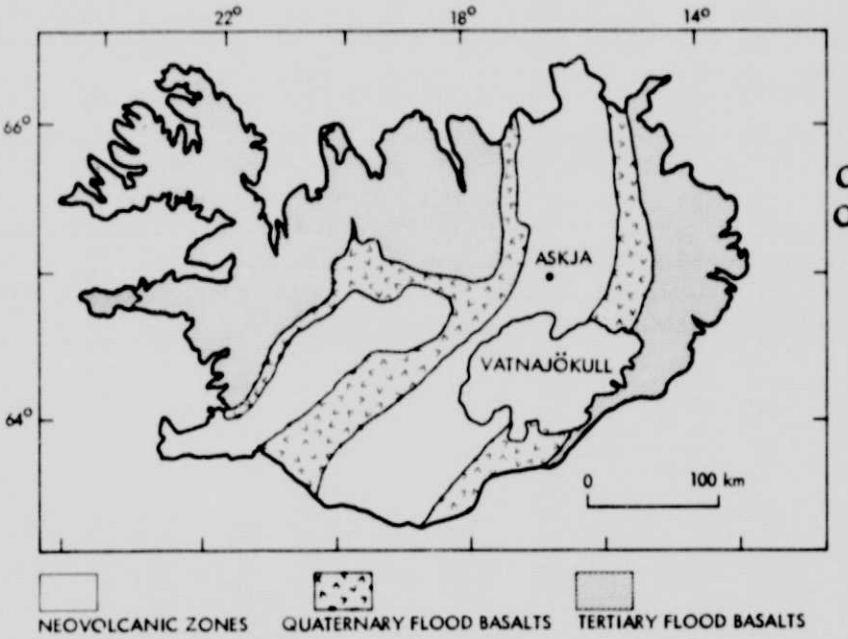

Fig. 1. Geologic map of Iceland (from Williams et al., 1973)

Askja Caldera, an active volcanic center, is located within the median zone in north-central Iceland. The caldera lies within the Dyngjufjöll massif at approximately 65°03′N, 16°55′W. The massif consists of late Pleistocene and Holocene palagonite tuffs and breccias and basaltic lavas (Thorarinsson and Sigvaldason, 1962). Early eruptions of Askja, centered along fissures near the present-day caldera rim, accompanied the postglacial uplift of Dyngjufjöll. Some of the early

lavas formed portions of the Útbruni lava field to the north and the Vikursandur lava field to the east of Askja. Other lavas flowed south and formed a plain between Askja and the Dyngjujökull icecap. These lavas also formed the floor of the precaldera cauldron (Bemmelen and Rutten, 1955). The Askja Caldera was formed during the final stages of deformation of Dyngjufjöll. Basaltic lava poured out from the marginal fractures at the western and southwestern sides of Askja and covered most of the caldera floor after caldera subsidence.

Askja has erupted four times since 1870. In 1875, a large pyroclastic eruption formed the crater Víti in the northeastern corner of the caldera. After the 1875 eruption, caldera subsidence created Öskjuvatn, which is 11 km^2 in area (Thorarinsson and Sigvaldason. 1962). Basaltic eruptions occurred twice between 1921 and 1929, both within and outside of the caldera. First, four small flows were produced between 1921 and 1923: Batshraun (1921), Myvetningahraun (1922), and two small flows in the southeast corner of Askja (1923); then, between 1924 and 1929, the large flow located south of Askja poured out from a 6-km-long fissure on the southern flank of the Dyngjufjöll massif. In 1961, eruptions north of the caldera produced a basaltic lava that flowed eastward through a break in the caldera called Öskjuop (Thorarinsson and Sigvaldason, 1962; see Fig. 2).

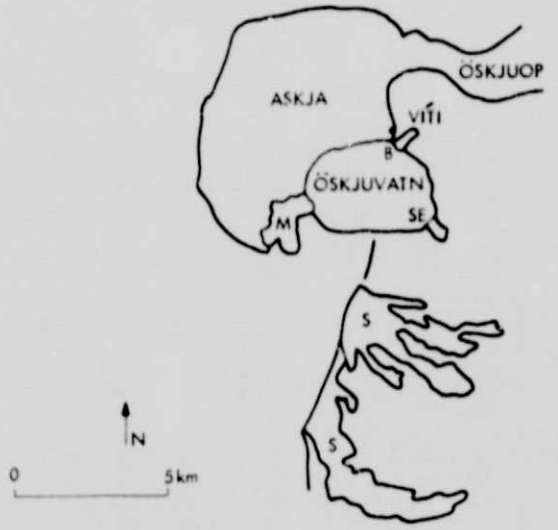

SE = 1923 FLOWS
S = 1924-1929 FLOWS
B = ATSHRAUN
M = MYVETNINGAHRAUN

Fig. 2. Geologic map showing historic flows in Askja region (modified from Bemmelen and Rutten, 1955)

SECTION III

RADAR IMAGES

The Askja Caldera region was chosen for a radar test site because of the diversity of surface textures and the paucity of vegetation. The radar images used in this study were obtained in July 1976 with a 25-cm-wavelength, side-looking airborne radar (see Table 1 for radar system specification). In this study, horizontally polarized radiation was transmitted and horizontally and vertically polarized backscatter were recorded. These modes are referred to as HH and HV, respectively. The radar equipment was flown aboard a NASA Convair 990 jet aircraft operated by the Airborne Sciences Office of Ames Research Center. The images were obtained at an altitude of 10,000 m. The look angle across the images varies from 0 to 45 deg. The flight line is shown in Fig. 3

Table 1. JPL radar system specifications

Operating frequency	1.2 Ghz
Operating wavelength	25 cm
Polarization	Horizontal transmit, horizontal receive; Horizontal transmit, vertical receive
Azimuth resolution	25 m
Range resolution, m	$15/\sin\theta$, where θ is the incidence angle which varies from $\theta = 0$ to $\theta = 45$ deg

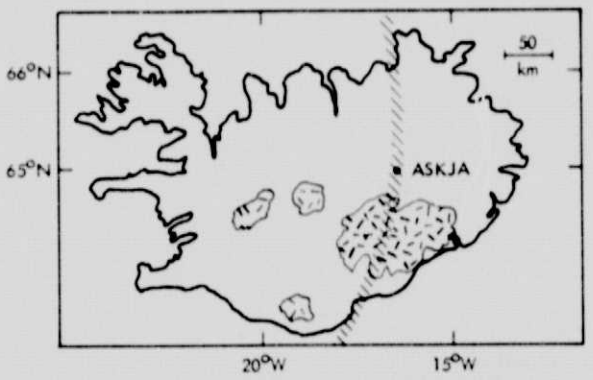

Fig. 3. Location map of Askja Caldera showing swath covered by radar

Synthetic Aperture Radar uses coherent microwaves to illuminate the surface below and to the side of the aircraft. The radar receiver detects the echo returned from the surface. The returned signal is mixed with a reference signal, and the resulting interference signal is recorded optically on film. The resulting signal film is developed on

the ground and illuminated with coherent light in an optical correlator. In this process, a visible-light replica of the radar waves received by the antenna is formed that recreates an image of the original terrain (see e.g., Jensen et al., 1977, for a detailed discussion). Radar image film can be printed as photographs or digitized for computer processing. Examples of HH (like-polarized) and HV (cross-polarized) images are shown in Figs. 4 and 5.

Fig. 4. Like-polarized (HH) radar image of Askja Caldera

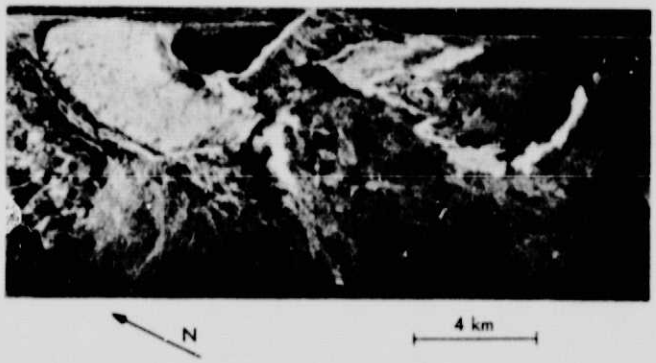

Fig. 5. Cross-polarized (HV) radar image of Askja Caldera

The bright line at the top of the images is the return from directly below the aircraft (nadir), where the look angle = 0 deg. Geometric distortions in the images include compression of the image near nadir, radar foreshortening, and shadowing. Radar shadows occur on the side of a terrain feature most distant from the transmitter because the radiated energy does not pass through objects (Fig. 6). Radar foreshortening occurs in areas with topographic relief when radar waves are reflected from sloping surfaces. Radar layover, an extreme case of foreshortening, occurs when the top of a feature is imaged before the bottom (Fig. 7). Steeply sloping surfaces had to be excluded from the Askja study because the radar did not portray reflectivity information accurately as a result of geometric distortions in the images.

Although theories of backscattering from terrain are not well formulated, it is generally agreed that the terrain parameters which affect radar backscatter are surface roughness, surface slope, and dielectric properties (see the Appendix for a discussion of backscatter theory). One of the first empirical geologic investigations using radar images was undertaken by Schaber et al. (1976). In their study, radar

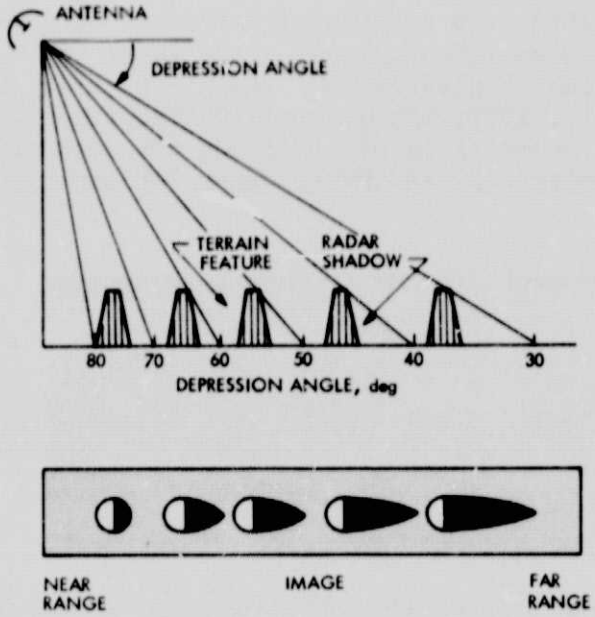

Fig. 6. Example of radar shadowing (from Sabins, 1978)

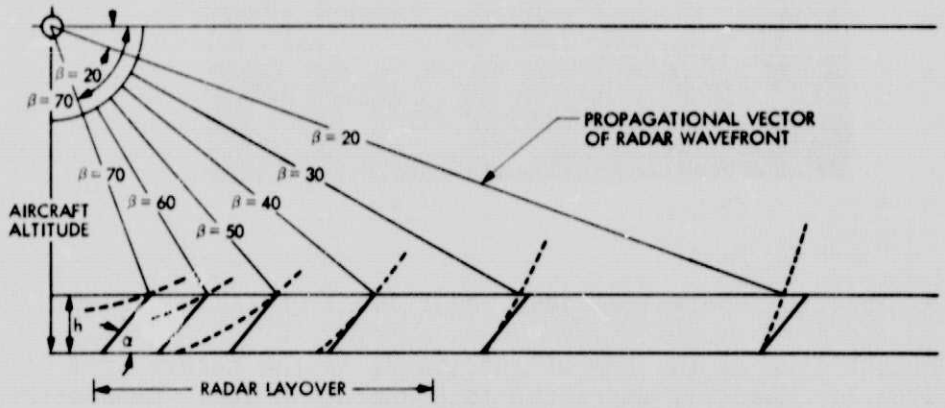

Fig. 7. Example of radar foreshortening and layover (from Reeves, 1975)

images of Death Valley were found to show distinctive variations in radar backscatter that could be correlated with changes in the surface roughness of different geologic units. The relationship between radar return power and surface roughness for seven backscatter units was evaluated by plotting a roughness parameter versus film density across a radar image that were converted to relative power. The roughness parameter was the sum of the average macrorelief (measured in centimeters), the average distance between macrorelief scattering facets (measured in centimeters), and the percent of the area covered by microroughness on the scale of $\lambda/10$, where λ is the radar wavelength (Table 2). The significant result

Table 2. Roughness parameters for backscatter units in Death Valley (from Schaber et al., 1976)

Backscatter unit	A Vertical macrorelief, cm	B Average distance between macrorelief facets, cm	C Percent area covered by microroughness, 1/10	(A+B+C) Roughness parameter	Relative power, dB
1	49.0	60.0	100.0	209.0	0.0
2	29.0	44.0	97.0	170.0	-0.4
3	6.0	15.0	20.0	42.0	-2.4
4	12.0	10.0	40.0	62.0	-3.0
5	1.5	6.0	15.0	22.5	-4.4
6	1.0	2.0	8.0	11.0	-4.5
7	0.2	2.0	0.0	2.2	-5.3

displayed by the graph of roughness parameter versus relative power was a change in slope that was interpreted to show a transition in backscatter behavior between a unit with vertical relief of 12 cm and a unit with vertical relief of 1.5 cm (see Fig. 8).

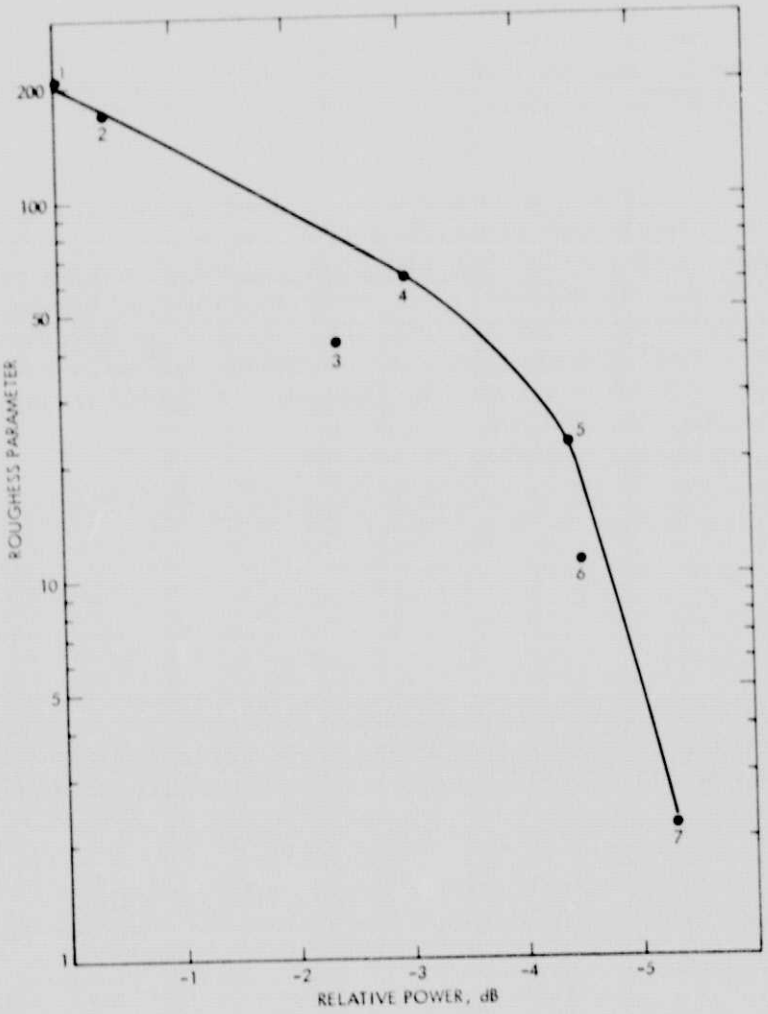

Fig. 8. Graph of surface roughness parameter versus relative power for backscatter units in Death Valley (from Schaber et al., 1976)

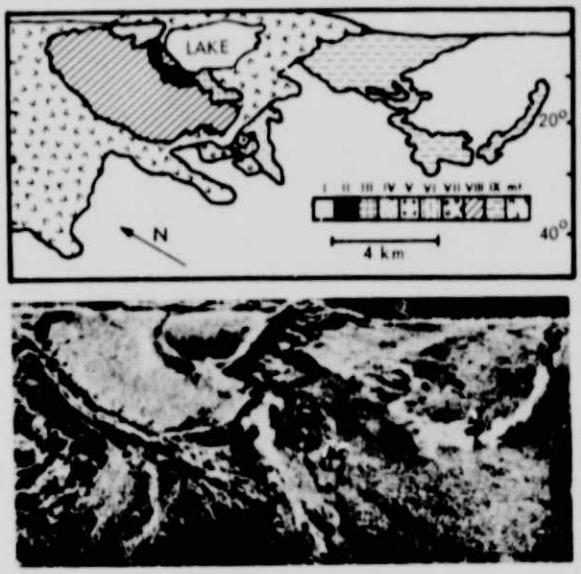

Fig. 9. Backscatter Units I-IX determined from radar images of Askja Caldera (Unit mt represents palagonitic breccias of Dyngjufjöll massif; from Malin et al., 1978.)

Nine backscatter units were distinguished on the Iceland radar images (Fig. 9). Roughness parameters were estimated for six of the backscatter units using data obtained from ground photographs (Table 3). The average vertical macrorelief, the average distance between macrorelief scattering facets, and percent area covered by microroughness were estimated from ground photographs which included scales. Examples of some of the photos used are shown in Fig. 10. Additional ground photographs are presented in Section V.

Table 3. Roughness parameters estimated from ground photographs and average DN values for Backscatter Units I-VI in Askja region (Units VII-IX were excluded because of insufficient data.)

Beckscatter unit	A Vertical macrorelief, cm	B Average distance between macrorelief facets, cm	C Percent area covered by microroughness, $\lambda/10$	(A+B+C) Roughness parameter	Average DN	Relative power, dB
I	15	10	90	115	190	-2.1
II	3	10	35	48	155	-4.0
III	25	15	100	140	210	-1.1
IV	20	25	90	135	230	0.0
V	30	30	40	100	165	-3.4
VI	5	5	5	15	130	-5.3

Fig. 10. Examples of ground photos obtained in Askja region (Scale marker = 25 cm; photographs by M.C. Malin.)

Figures 11 through 15 are plots of digital number (DN) versus sample location along a given line. The DN values are linearly related to power received by the radar since the data were scanner corrected. A linear transformation was applied to the DN values in order to make them proportional to relative powers used by Schaber et al. (1976). A graph of roughness parameters versus relative power for the Iceland data is shown in Fig. 15.

The brightness values used in the Death Valley study were determined at a constant look angle along one scan line. The Iceland scan lines were at varying look angles because of the relative locations of the backscatter units. The brightness values of two units that span the width of the image were compared at varying look angles. No significant variation of DN values with look angles could be seen within the accuracy of measurements. The lack of statistical data probably results in the greatest errors. In the Iceland study, roughness parameters for the backscatter units are based on stereographic ground photos and field observations, while the roughness parameters in Death Valley represent averages of many field measurements.

With these limitations, the graph of roughness parameter versus relative power for backscatter units in the Askja region shows trends similar to those found in the Death Valley study. A break in slope occurs between Unit V (average surface height = 30 cm) and Unit II (average surface height = 3 cm). There are insufficient backscattering units in the Askja region to determine the breakpoint more precisely.

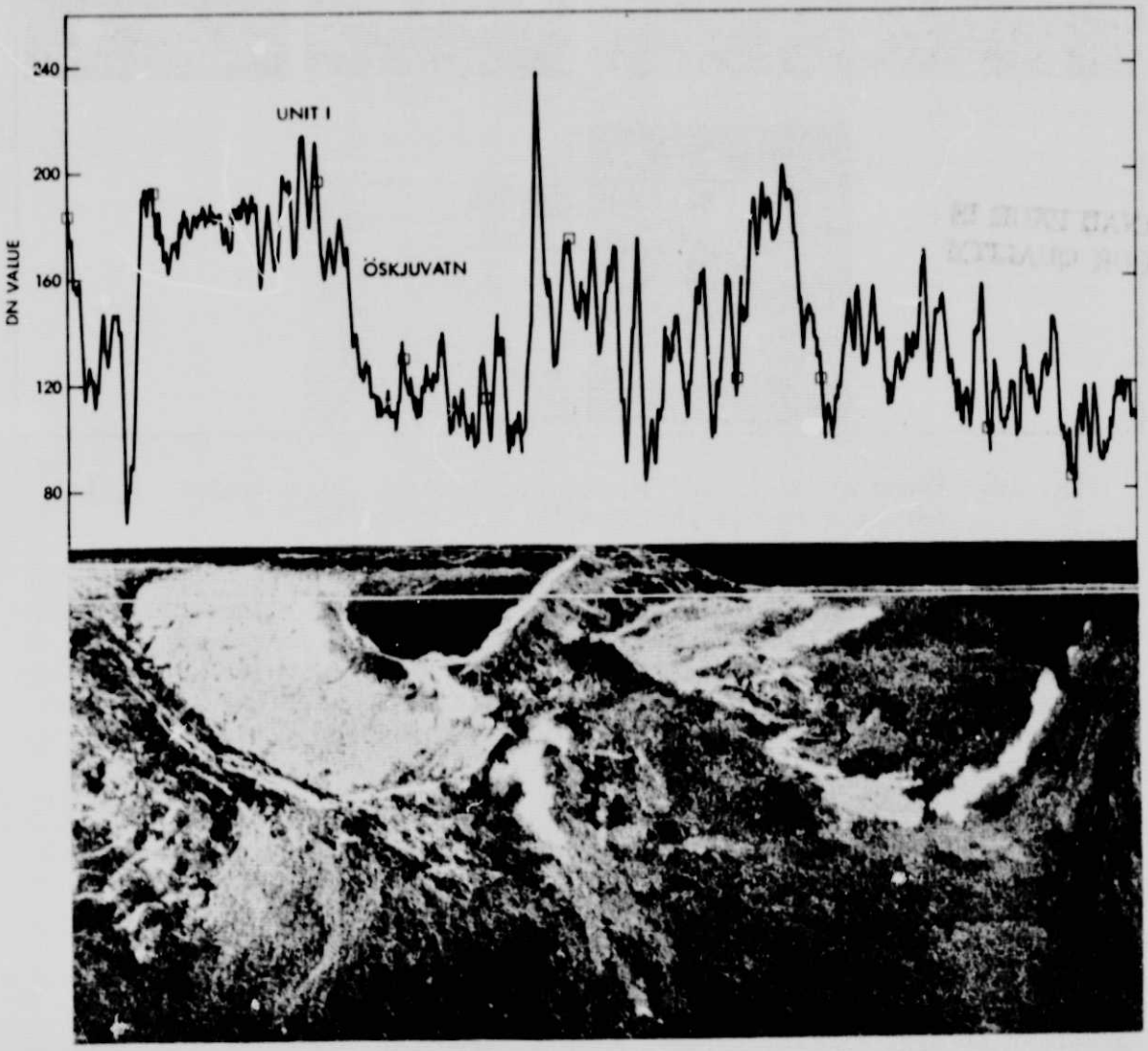

Fig. 11. DN values at sample locations along line 100 and radar image showing line and sample locations

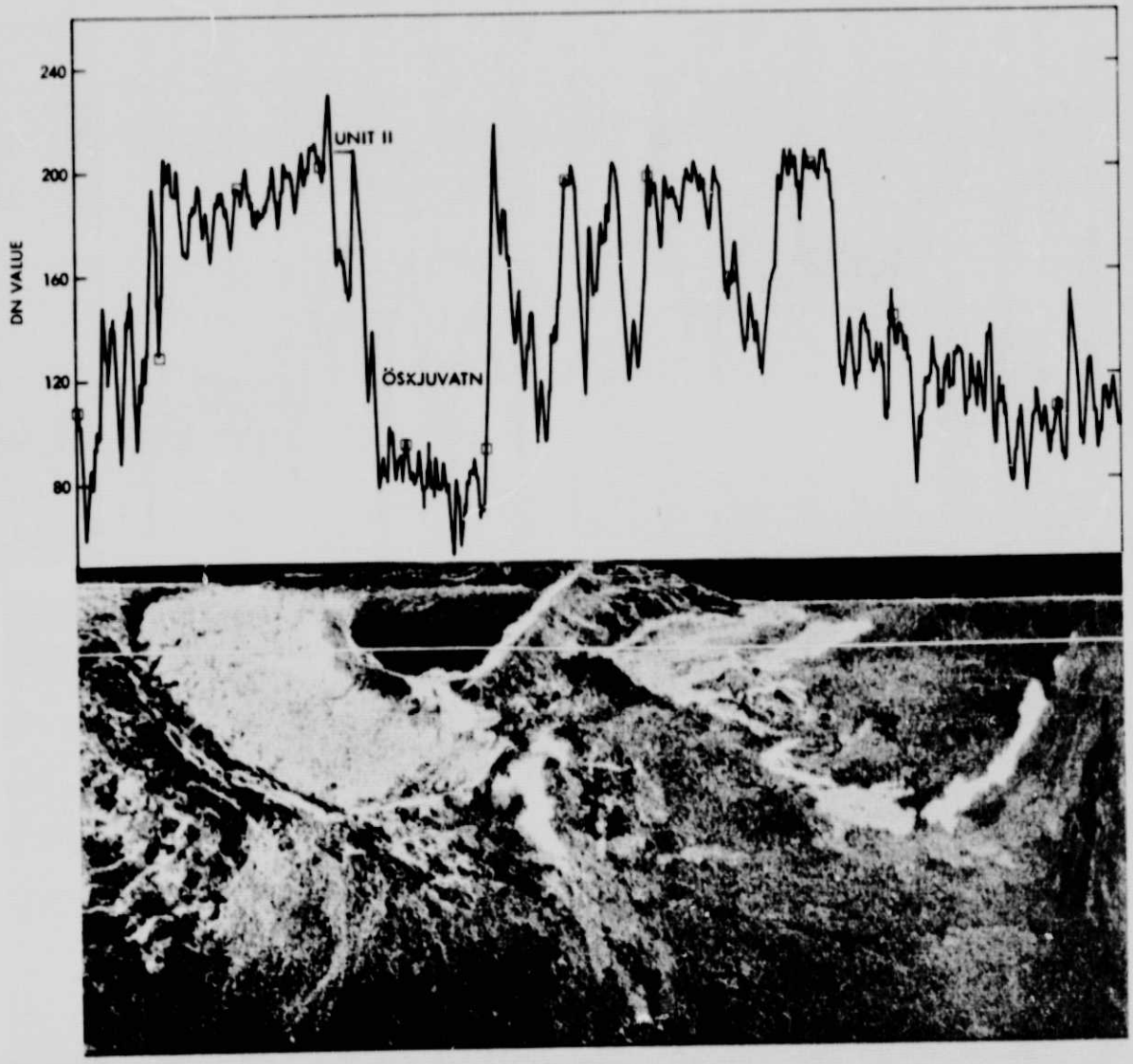

Fig. 12. DN values at sample locations along line 175

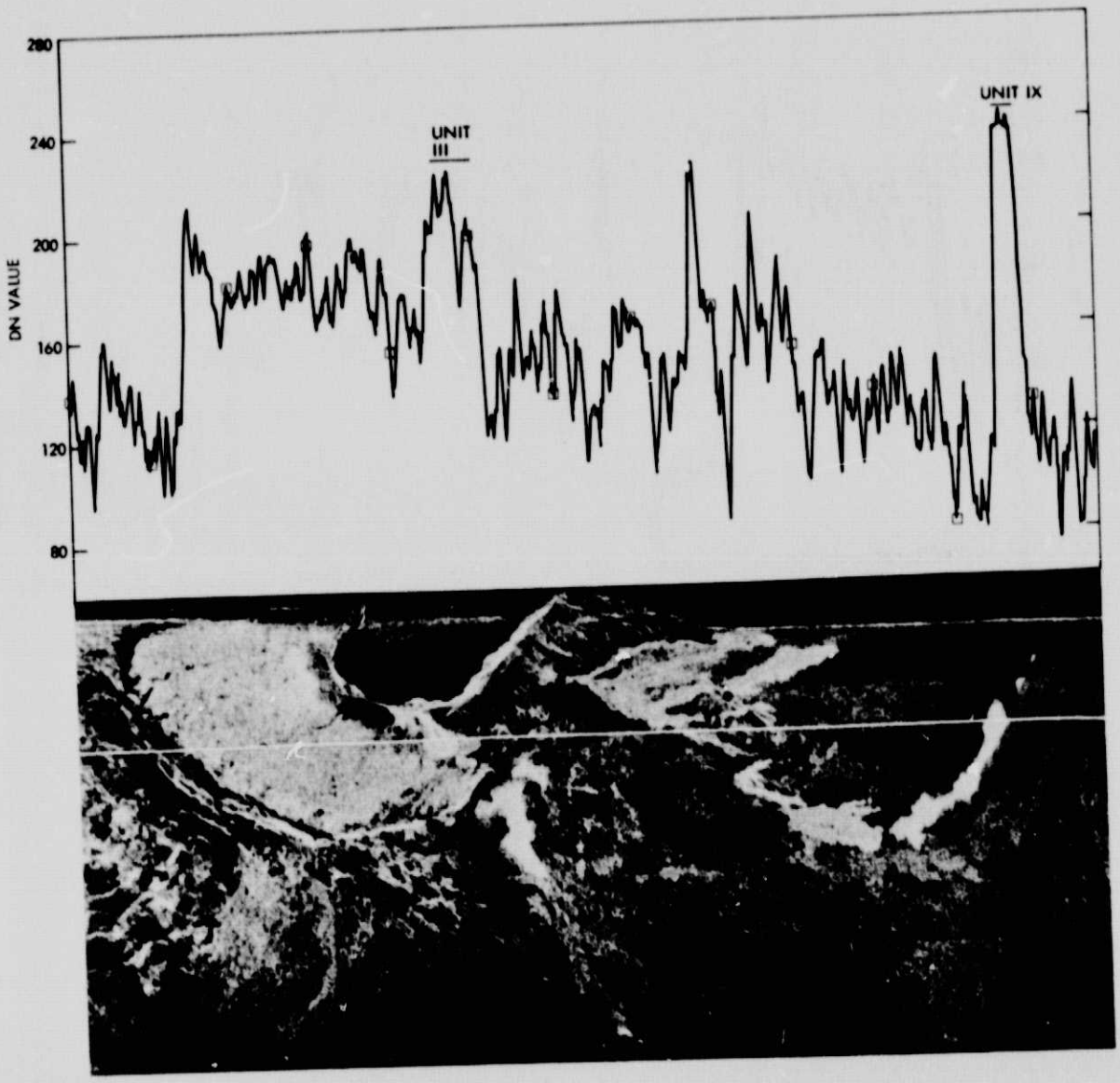

Fig. 13. DN values at sample locations along line 300

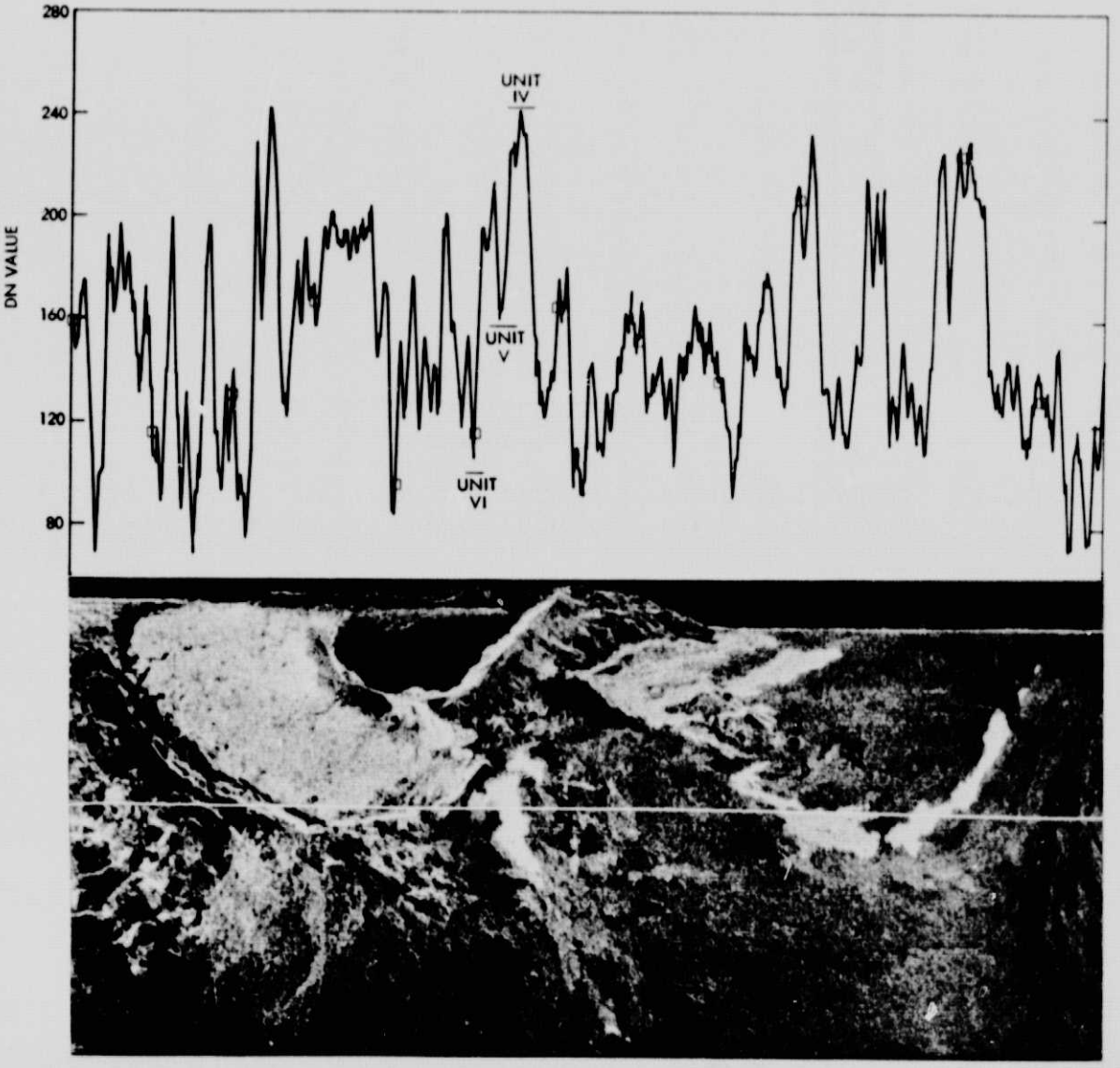

Fig. 14. DN values at sample locations along line 450

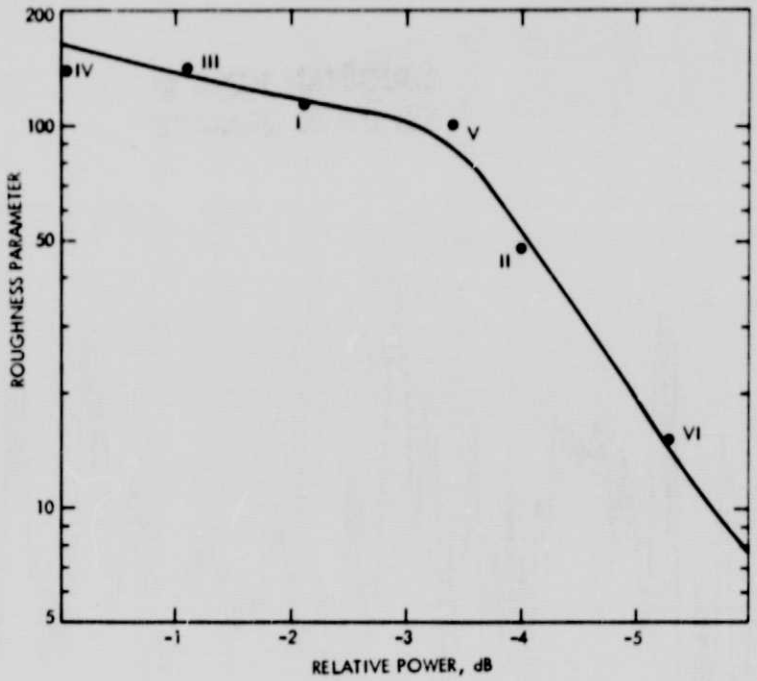

Fig. 15. Graph of roughness parameter versus relative return power for Backscatter Units I-VI in the Askja Caldera test site

Although the Death Valley and Iceland images demonstrate that changes in surface roughness can be correlated with variations in grey tones on a single polarization image, multiple polarization images must be used to determine the overall roughness spectrum of a surface (Daily et al., 1978).

SECTION IV

COMPUTER IMAGE PROCESSING

Digital processing of the Iceland images was performed using the facilities of the Image Processing Laboratory (IPL) at the Jet Propulsion Laboratory. The central computer at IPL is an IBM 360/65. The software system manipulates digitized data and creates a processed image that can be converted into a photograph. Computer processing of the Iceland images involved many of the techniques described by Daily et al. (1978), including digitization, scanner correction, registration, and differencing and ratioing.

Radar images were digitized from image film using a high-resolution microdensitometer that recorded the amount of light transmitted through image film transparencies at selected locations in a rectangular grid. In this process, a digital number that corresponds to a grey level in the original image is assigned to each picture element. The DN values range from 0 (black) to 256 (white). The spacing at which the transparency is scanned determines the pixel size. For the Iceland data, film transparencies were scanned using an aperture that recorded the average film density over 40-μm squares spaced 40 μm apart, which makes each pixel correspond to 20 x 20 m on the ground.

The power of the radar return is a more linear function of film density than of the transmission recorded as DN values. Because the IPL film recording hardware exposes film so that film density is linearly related to DN, it was necessary to perform an intensity transformation on the digitized radar data in order to achieve linearity with the film density of the output.

In order to analyze multiple data sets of the same areas on the ground, digital images were spatially transformed to bring corresponding surface features to the same location in each image. This registration was performed by geometrically transforming one image so that features in it overlaid the corresponding features in the reference image. The first step in the registration process was to manually select features which could be identified in each image (tiepoints). A polynomial that related the tiepoint locations on each image was then calculated. The coefficients of the polynomial were adjusted to minimize the squared distance between the manually selected tiepoints and the locations determined by the polynomial. In many cases, it was difficult to find features that could be precisely located in each image. The discrepancies between tiepoint locations that were measured and those determined by the calculated polynomial were checked in order to identify incorrect tiepoints and to assess the accuracy with which the computed polynomial modeled the actual spatial difference between the two images. In addition, the order of the polynomial was varied and discrepancies were reevaluated to determine the form of the polynomial that best fit the tiepoints. The polynomial was evaluated at control points in a square grid in the reference (master) image. Corresponding locations on the other (slave) image were determined using bilinear interpolation based upon the four ambient control points. Geometrically transformed slave images were generated by assigning the estimated location in the slave image to each master image

location. Figure 4 is a like-polarized (HH) master image. Figure 5 is a geometrically transformed cross-polarized (HV) image.

Difference and ratio images were generated by computing the difference or ratio of DN values of corresponding samples of registered images. The differences were displayed with zero difference translated to a DN of 128 (intermediate grey). A ratio equal to one is also displayed as intermediate grey (DN = 50 in this case). Figure 16 shows an example of an image which is the result of ratioing a like-polarized (HH) radar image to a cross-polarized (HV) radar image. Figure 17 is an example of an image which is the result of subtracting an HV image from an HH image. The digital form of the ratioed and differenced data is presented graphically in Figures 18 and 19, which are plots of intensities (DN values) along a given line versus sample number (horizontal location).

Fig. 16. Polarization ratio image (HH/HV) of Askja radar images

Fig. 17. Polarization difference picture (HH-HV) of Askja radar images

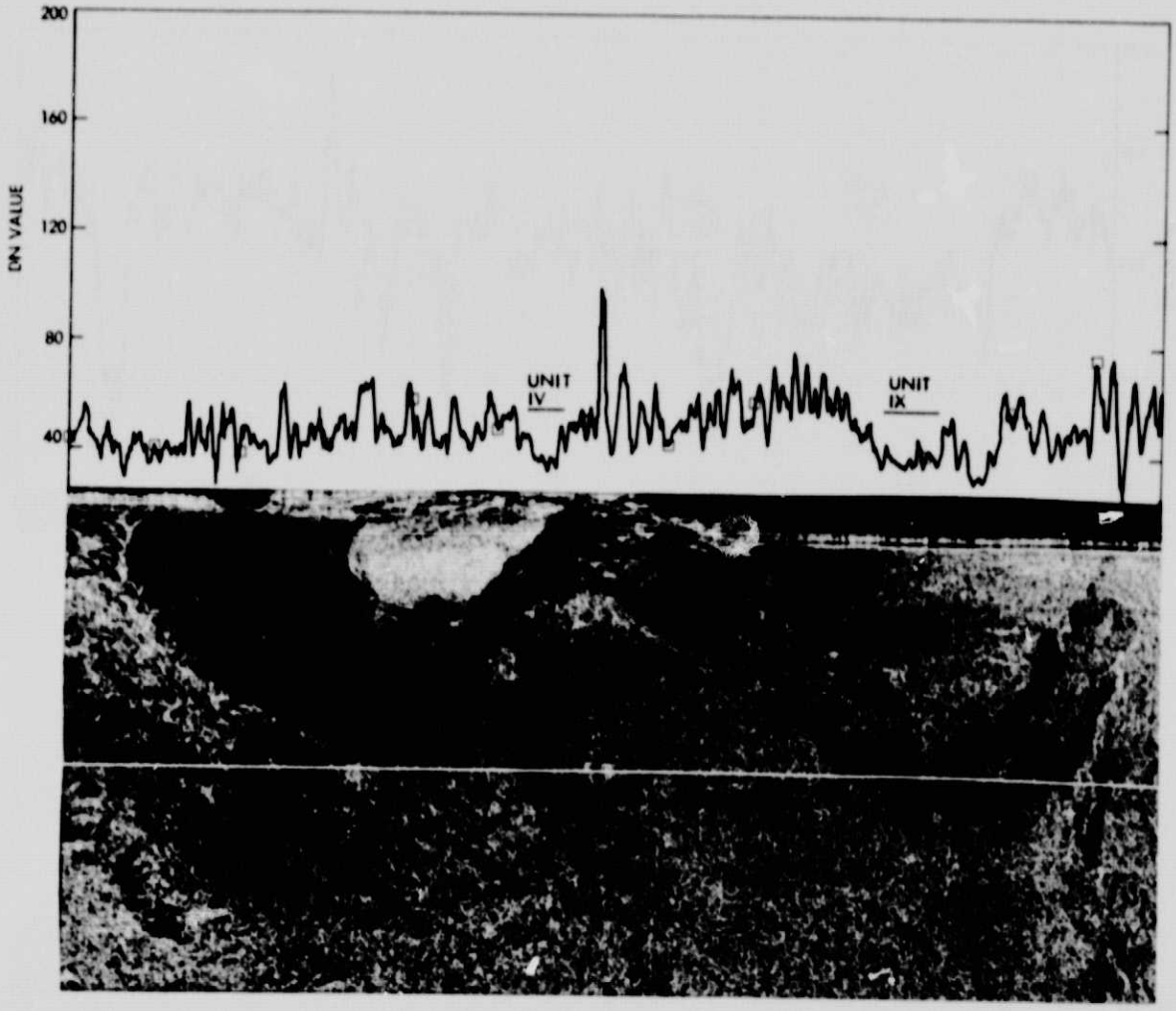

Fig. 18. DN values at sample locations along line 525 in polarization ratio image (HH/HV)

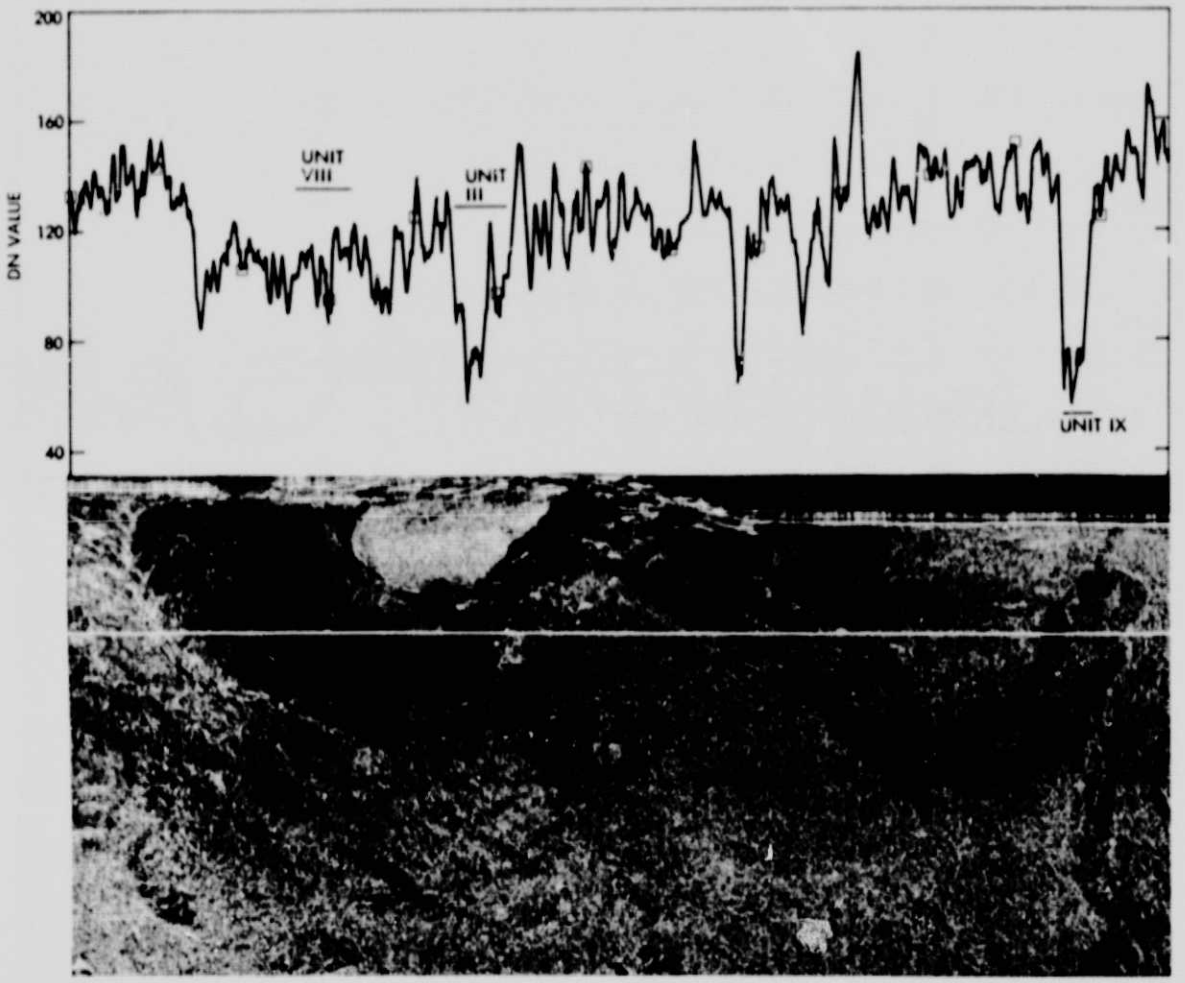

Fig. 19. DN values at sample locations along line 300 in polarization difference image (HH-HV)

SECTION V

RADAR RESPONSE TO SURFACE MATERIALS IN THE ASKJA CALDERA REGION

The overall roughness spectra of the radar backscatter units in the Askja region were predicted from multipolarized radar images based on studies in Death Valley (see, e.g., Schaber et al., 1976; Daily et al., 1978; and the Appendix). A field survey of the caldera was undertaken to check the accuracy of the preliminary analysis. Areas visited included the caldera floor, the southern rim, and a portion of the southern flank of the caldera. The traverse followed the route outlined in Fig. 20. Nine areas with mappable differences were chosen to be field checked prior to the traverse. These units are identified in Figs. 9 and 20. However, only eight of the nine areas could be field checked due to time limitations. Ground photography of both the overall surface characteristics and fine-scale detail were acquired for most areas, including oblique and vertical stereo pairs.

A. RADAR UNIT I (Figs. 21 and 22)

Unit I is characterized by a high radar reflectivity and a low polarization ratio (HH/HV) and difference (HH-VH). Based on Bragg and Rayleigh scattering models (see the Appendix), this unit was interpreted to have a surface of variable roughness with a predominance of scatterers greater than 3 cm in diameter. Field observations showed Unit I to consist of ash and pumice from the 1875 explosive eruption of the crater Víti. In less than 12 hours, the crater, then only 100 m wide, produced 2 cm^2 of rhyolitic pumice. The 1875 eruption was the only eruption that produced rhyolitic pumice in the Dyngjufjöll area (Wood et al., 1977). The surface of Unit I is littered with pumice blocks ranging from about 1 to 40 cm, which is consistent with predictions.

B. RADAR UNIT II (Figs. 23 and 24)

Unit II is characterized by an extremely low radar reflectivity. This low reflectivity and a polarization ratio of ~1 (shown as intermediate grey on Fig. 6) suggested a smooth surface with a small range in surface roughness. Field observations showed that Unit II consisted of ash and pumice from the 1875 Víti eruption. In some areas, deflation and dissection expose extensive deposits of finely bedded ash. The surface of these deposits consists of indurated ash less than 0.5 cm and numerous clasts of pumice approximately 0.5 to 6 cm in diameter. Deflation has left cobbles supported on ash pedestals.

The surface of Unit II was smoother than predicted from reflectivity data. This observation and field inspection indicate that moisture may be contributing to the radar signature by increasing the radar signal. The presence of moisture could also increase the depolarized return more than the like-polarized return because of the greater sensitivity of HV images to the surface dielectric constant (Daily et al., 1978). Although the depolarized return from Unit II is slightly brighter than the like-polarized return, this seems to be a minor effect. The effect of water on the reflectivity cannot be determined accurately since the amount of penetration of the radar and the resulting decrease in volume scattering

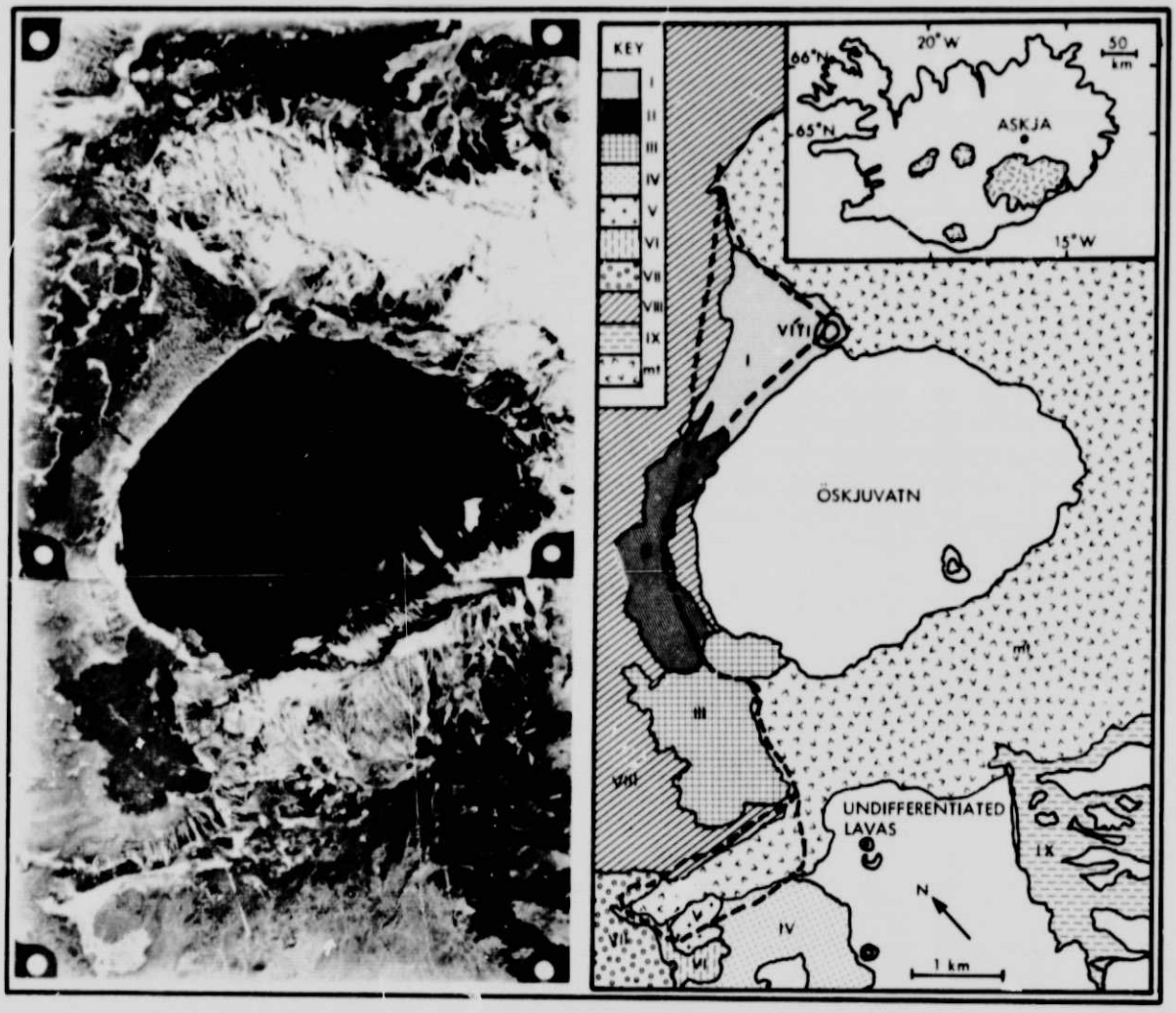

Fig. 20. Aerial photograph and map of Radar Backscatter Units I-IX showing traverse (dashed line) and ground photo locations (Unit mt represents palagonitic breccias of the Dyngjufjöll massif; from Malin et al., 1978.)

Fig. 21. Radar Unit I (looking west) showing pumice blocks from 1875 eruption of Vîti (Blocks range from 1 to 40 cm; photograph by M.C. Malin.)

Fig. 22. Closeup of Radar Unit I (photograph by M.C. Malin)

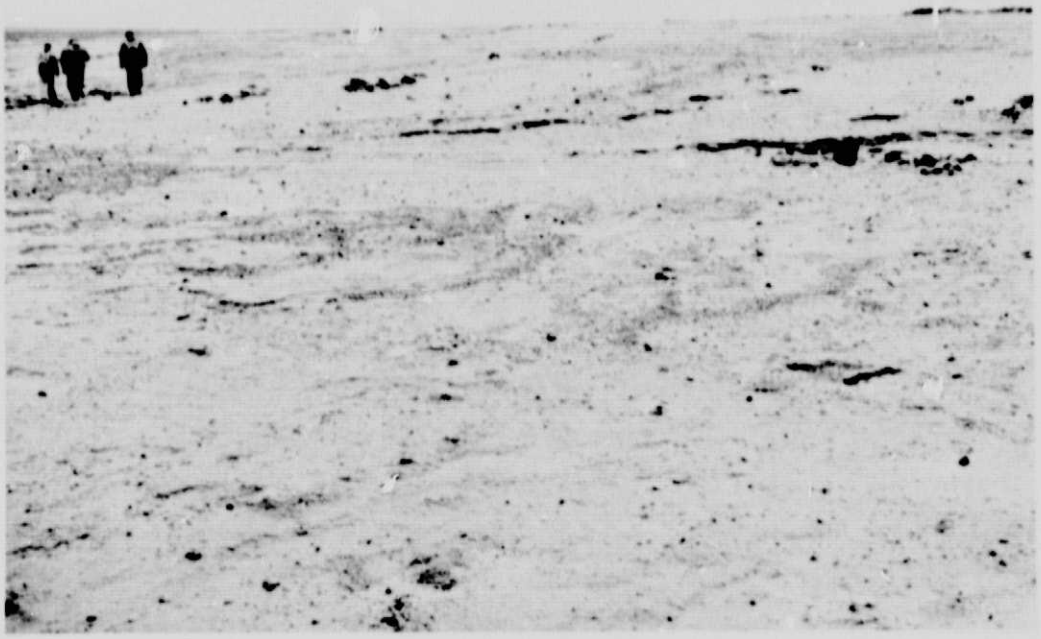

Fig. 23. Radar Unit II (looking west) showing ash and pumice from 1875 Víti eruption (Pumice clasts range from 0.5 to 6 cm; photograph by M.C. Malin.)

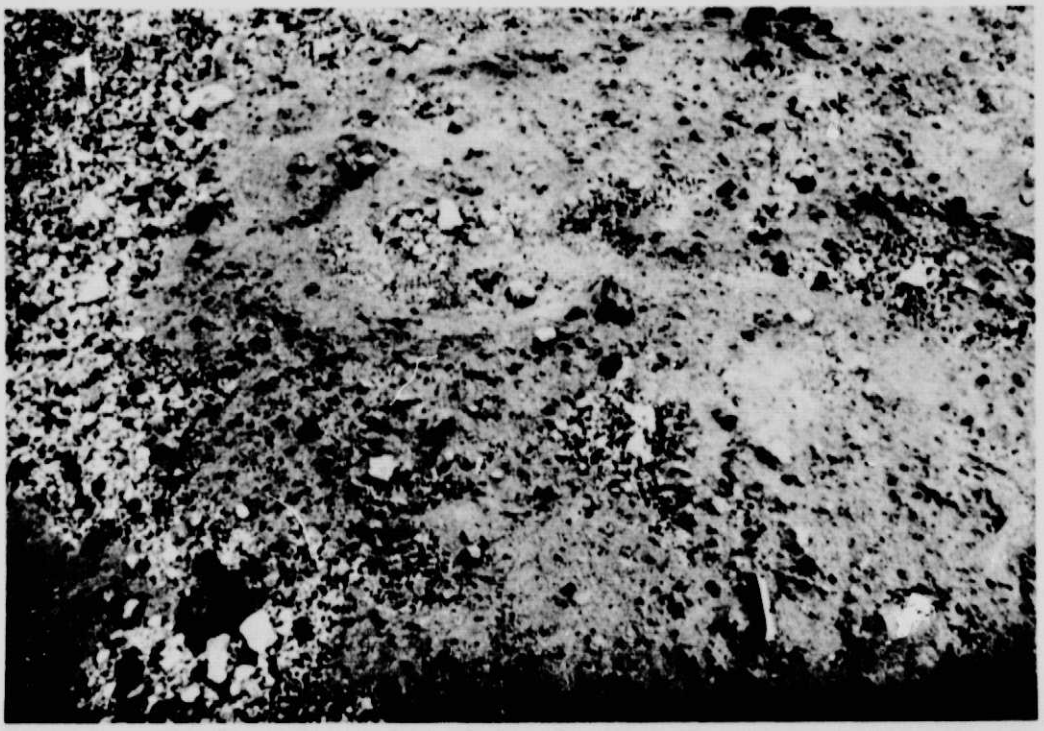

Fig. 24. Closeup of Radar Unit II (photograph by M.C. Malin)

cannot be ascertained with single-frequency, dual-polarization data.

C. RADAR UNIT III (Figs. 25 and 26)

Unit III could be easily distinguished on both the radar image and aerial photograph, and it is correlated with a geologic unit called Myvetningahraun (Bemmelen and Rutten, 1955). This unit clearly showed flow features. It was interpreted as an aa flow since the radar return was strong and the direct to cross-polarization ratio was low. Myvetningahraun, which is located in the southwest corner of Askja Caldera along the shore of Öskjuvatn, flowed from a north-south fissure in the caldera floor near Suderskard in November 1922. The flow has an area of 1.75 km^2 and an average thickness of 5 m. Field observations showed that Unit III does have an aa texture (apalhraun, in Icelandic), consisting of broken slabs ranging in size from a few centimeters to a few meters. Several areas of underlying Unit II ash and pumice show through Myvetningahraun as a result of incomplete flooding of lava. These windows are dark patches in the flow on the radar images due to a difference in surface roughness, and they are light patches on the aerial photo due to a difference in albedo between Units II and III.

D. RADAR UNITS IV AND V (Figs. 27 and 28)

Unit IV was the second-brightest radar return seen in the Askja area. It was brighter than Unit III, which was a very rough aa flow. The low polarization ratio and difference values also indicated a greater range in roughness than for Unit III. The reflectivity and polarization ratio of Unit V suggested a surface somewhat smoother than those of Units III and IV. Field inspection revealed both lavas to be the same lava flow. Both are lichen-covered aa, but Unit V is partially covered with volcanic ash. The extremely high radar return from Unit IV may result in part from the surface morphology of a hummocky, steep-walled ridge-and-trough topography with spacings of 2-3 m and relief of 1 m. In addition, the lichen cover may contribute to the greater reflectivity because of its higher dielectric constant. The low direct to cross-polarization ratio may also be partially caused by the relatively high dielectric constant of the lichen enhancing the HV return. The effect of lichen cover cannot be determined accurately. Because the dielectric constant increases with an increase in moisture content, the same problem exists as in Unit II, that dielectric effects cannot be separated from roughness effects on single-frequency, dual-polarization images.

The return from Unit V is lower than that from Unit IV because of the increase in ash cover and the resultant reduction in surface roughness. A slight albedo difference can be seen between Units IV and V on the aerial photo that can be correlated with a difference in surface roughness on the radar images.

E. RADAR UNIT VI (Figs. 29 and 30)

Unit VI is characterized by the lowest reflectivity of all the surfaces studied. This unit was interpreted to be smooth. Field observations showed that Unit VI consists of a cobble and pebble pavement cemented by ash, which results in only centimeter-scale relief.

Fig. 25. Radar Unit III (looking northeast) — Myvetningahraun (Blocks range in size from a few centimeters to a few meters; photograph by M.C. Malin.)

Fig. 26. Closeup of Radar Unit III (photograph by M.C. Malin)

Fig. 27. Radar Unit IV (looking east) showing lichen-covered aa lava with hummocky surface morphology (photograph by M.C. Malin)

Fig. 28. Radar Unit V (looking west) showing ash-covered aa lava (Same age as Unit IV; photograph by M.C. Malin.)

Fig. 29. Radar Unit VI (looking southwest) showing cobble and pebble pavement cemented by ash (photograph by M.C. Malin)

Fig. 30. Closeup of Radar Unit VI (photograph by M.C. Malin)

This surface produced a near-specular reflection away from the radar. The signal returned to the antenna is low in both polarization modes because the roughness elements are much smaller than the wavelength of the radar. Unit VI can easily be distinguished on the aerial photo by its high albedo.

F. RADAR UNIT VII (Figs. 31 and 32)

The lavas outside the caldera rim to the northeast and east are difficult to differentiate on the radar images. Unit VII has indistinct boundaries on the radar images. The overall reflectivity indicated a surface of up to 25 cm relief and a wide range in surface roughness. In the field, the unit consists of aa lava and ash cover. Approximately 20% of the surface consists of cobble-sized fragments.

G. RADAR UNIT VIII (Fig. 33)

Unit VIII, which occupies the floor of the caldera, is bright in both the like- and cross-polarized images. The low polarization ratio and low difference value for this unit indicated a wide range in surface roughness. In the field, these lavas are often comparable to those of Unit III in roughness, although portions have significant ash cover from the 1875 eruption. A few outcrops of Unit VIII occur along the edge of Öskjuvatn. These are completely separated from the main body of Unit VIII by the pumice and ash of Unit II that overlies Unit VIII.

H. RADAR UNIT IX (no figure available)

Unit IX displays the best example of lava flow morphology seen in the Askja images. The high reflectivity indicated a rough aa surface. The alignment of flows is evidence of a linear vent. The highest reflectivity in the Askja area and the lowest direct to cross-polarized ratio occur at the extreme south end of the flow. This area was not visited during the field study because of logistical problems. Unit IX can be distinguished on the aerial photograph and can be correlated with a geologic unit. According to Thorarinsson and Sigvaldason (1962), this flow erupted between 1924 and 1929. Aerial photographs and personal accounts of visits to the flow by other investigators suggest a strong similarity between Unit IX and Unit III.

I. CONCLUSIONS

In the Askja test site, radar provided additional information to aerial photography since differences in grey tones could be correlated with variations in surface roughness. For example, a slight albedo difference can be seen between Units IV and V on the aerial photograph that can be correlated with a difference in surface roughness on the radar images.

There was good agreement between predicted surface roughness of backscatter units based on computer-enhanced like- and cross-polarized radar images and surface roughness observed in the field. In some cases, variations in surface roughness could be correlated with previously mapped geologic units. The ability to differentiate among lithologies

Fig. 31. Radar Unit VII (looking west) showing aa lava and ash cover (Clasts range from 10 to 75 cm; photograph by M.C. Malin.)

Fig. 32. Closeup of Radar unit VII (photograph by M.C. Malin)

Fig. 33. Radar Unit VIII overlain by Unit II (looking southwest; photograph by M.C. Malin)

using radar is particularly valuable in areas where field work is impossible, on earth as well as other planets. For example, a good understanding of radar backscatter will aid in interpreting the geology of Venus from images returned by the proposed Venus Orbiting Imaging Radar (VOIR).

SECTION VI

DISCUSSION

Although single-frequency, dual-polarization images used in the Iceland study provided information regarding the average heights of surface irregularities and the overall roughness spectra of several geologic units, additional frequency and polarization modes would make it possible to discriminate among more roughness units. Multifrequency imaging would make it possible to differentiate among more units since the transition between diffuse and specular reflection (see the Appendix) is wavelength-dependent, according to Rayleigh scattering models. Multifrequency imaging could also be used to determine the contribution of subsurface multiple scattering because the ratio of a cross-polarized image to a direct polarized image is constant as a function of frequency when multiple scattering is negligible (Daily et al., 1978). Additional polarization modes would make it possible to differentiate among more units since simultaneous analysis of HH/VV images and HH, VV, and HV images should allow separation of roughness effects from topographic and dielectric effects (Daily et al., 1978). The radar interpretation techniques, such as those used in the Death Valley and Iceland studies, are still being developed. Future studies will concentrate on relating surface roughness data to specific rock types. This would involve correlating roughness spectra derived from multipolarization and multifrequency radar data with the texture of primary surfaces as well as texture produced by physical weathering of the rock.

APPENDIX

THEORETICAL BASIS FOR BACKSCATTERING STUDIES

The average power received by a radar antenna (P_R) is given by the Radar Equation:

$$P_R = \frac{P_T G^2 \lambda^2 \sigma^\circ A}{(4\pi)^3 R^4}$$

where

P_T = transmitted power

G = gain of the antenna

σ° = normalized backscatter (fraction of power reradiated from a point)

A = area of illumination

R = distance between antenna and scatterer

λ = radar wavelength

The normalized backscatter is a function of radar system properties, including polarization, depression angle, and wavelength, and terrain parameters, including dielectric properties, surface roughness, and terrain slope. The intensity of a radar return is determined by the same parameters when all other terms of the radar equation are held constant.

1. Depression Angle

Depression angle is the angle at which a radar pulse is sent out from the aircraft, measured from horizontal. It is the complement of the angle of incidence. Look angle (= incidence angle) is measured from vertical. Therefore, a depression angle of 90 deg and a look angle of 0 deg are both perpendicular to the surface. The transition between specular and diffuse reflection from a surface is a function of depression angle and surface roughness. The Rayleigh criterion predicts that scatterers with surface heights greater than $\lambda/(8 \sin \theta)$, where λ is the radar wavelength and θ is the angle of incidence, will result in diffuse reflection (Fig. A-1). The magnitude of the normalized backscatter coefficient generally increases with decreasing incidence angle. However, it becomes independent of incidence angle if the surface is rough with respect to radar wavelength (see Fig. A-2).

2. Wavelength

Variations in the radar return that are wavelength-dependent are directly related to surface roughness and dielectric properties. The Rayleigh criterion predicts that a given surface will appear rougher at shorter wavelengths. Attenuation of the radar signal is a function of radar wavelength and the complex dielectric constant of a material. The depth of penetration of radar below the surface (skin depth) varies directly with radar wavelength and inversely with the imaginary part of the dielectric constant.

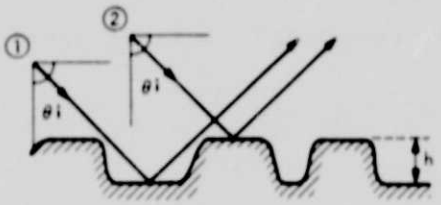

Fig. A-1. Geometry of Rayleigh criterion (h = surface height, θ = angle of incidence; from Schaber et al., 1978.)

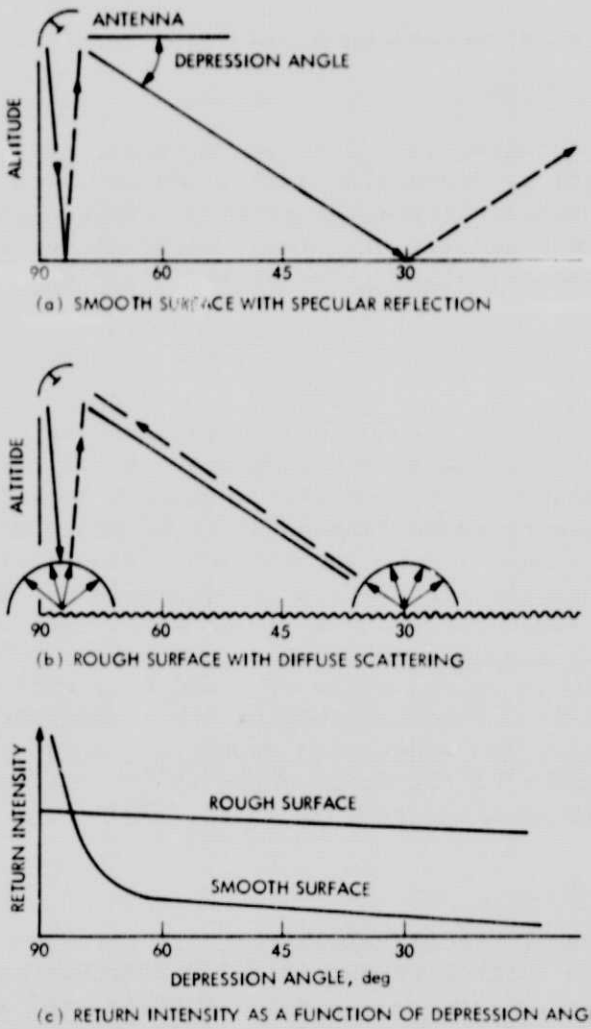

Fig. A-2. Radar returns from smooth and rough surfaces as a function of depression angle (from Sabins, 1978)

3. Polarization

A like-polarized return is recorded when a horizontally polarized radar signal is transmitted and a horizontally polarized signal is received or when a vertically polarized signal is transmitted and a vertically polarized signal is received. These modes are called HH and VV, respectively. A cross-polarized or depolarized return is recorded when a horizontally polarized signal is transmitted and a vertically polarized image is received or when a vertically polarized signal is transmitted and a horizontally polarized image is received. These modes are called HV or VH.

Different types of scatterers will produce different types and degrees of depolarization. It is possible to infer what type of scatters are responsible for an observed type of depolarization (Beckmann, 1968). Two mechanisms which cause depolarization are (1) multiple scattering as a result of target surface roughness and (2) volume scattering due to nonhomogeneities within the skin-depth of the target surface (Sabins, 1978).

4. Terrain Parameters

The backscatter cross-section of a slightly rough surface has been described by Valenzuela (1967 and 1968). The expressions for the direct polarization case (HH) and the cross-polarization case (HV) are:

$$\sigma_{HH} = AW(K_x,K_y) + CI$$

$$\sigma_{HV} = DW(K_x,K_y) + EI$$

$$A = 4\pi\beta^4 \cot^4 \theta_i(\alpha^2 \cos^2 \delta T_1 + \sin^2 \delta T_2)^2$$

$$C = 2\pi\beta^8 \cot^4 \theta_i \sin^2 \theta \sin^2 2\delta T_3^2$$

$$D = \pi\beta^4 \cot^4 \theta_i \alpha^2 \sin^2 2\delta(T_2 - T_1)^2$$

$$E = 2\pi\beta^8 \cot^4 \theta_i(\alpha^2 \cos^2 \delta - \sin^2 \delta)^2 T_3^2$$

$$T_1 = \frac{\varepsilon - 1}{\left[\cos\theta \cos\delta + \sqrt{\varepsilon - \sin^2\theta_i}\right]^2}$$

$$T_2 = (\varepsilon - 1)\frac{(\varepsilon - 1)\sin^2\theta_i + \varepsilon}{\left[\varepsilon \cos\theta \cos\delta + \sqrt{\varepsilon - \sin^2\theta_i}\right]^2}$$

$$T_3 = (\varepsilon - 1)^2 \frac{\sqrt{\varepsilon - \sin^2\theta_i}}{\cos\theta \cos\delta + \sqrt{\varepsilon - \sin^2\theta_i}}$$

$$I = \int_{-\infty}^{\infty} dp \int_{-\infty}^{\infty} dg\, p^2 g^2 \frac{W(p - \beta \sin\theta, g)W(p + \beta \sin\theta, g)}{|d(p,g)Dpg|^2}$$

$$d(p,g) = \sqrt{\beta^2 - (p^2 + g^2)\sin^2\theta} + \sqrt{\varepsilon\beta^2 - (p^2 + g^2)\sin^2\theta}$$

$$Dpg = \sqrt{\beta^2 - (p^2 + g^2)\sin^2\theta}\sqrt{\varepsilon\beta^2 - (p^2 + g^2)\sin^2\theta} + (p^2 + g^2)\sin^2\theta$$

Where

δ = tilt angle perpendicular to the plane of incidence

θ = look angle

θ_i = actual incidence angle

α = $\sin\theta$

ε = dielectric constant

α_i = $\sin\theta_i$

β = $2\pi/\lambda$

λ = radar wavelength

$w(p,g)$ = energy spectral density of the surface

For the geometry of the equations, see Fig. A-3.

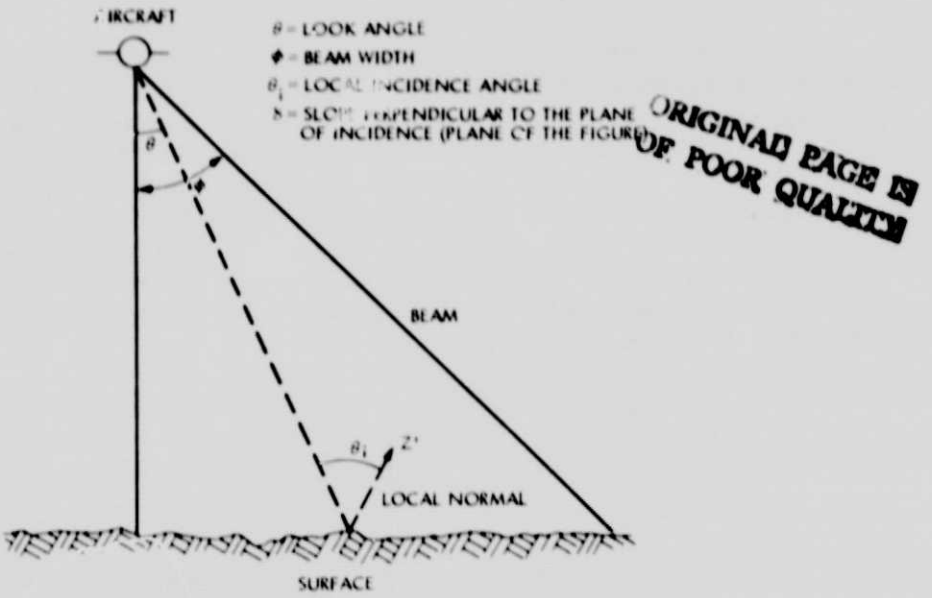

Fig. A-3. Geometry for backscatter equations (from Daily et al., 1978)

These expressions can be used to help understand the behavior of the different backscatter cross-sections as a function of surface characteristics (Daily et al., 1978).

4. The Effect of Surface Roughness

The term $W(K_x,K_y)$ corresponds to the single Bragg scattering from the spectral component which satisfies the Bragg condition, $\Lambda = \lambda/(2 \sin \theta)$, where Λ = surface roughness wavelength, λ = radar wavelength, and θ = look angle. Only one spectral component of the surface satisfies the Bragg condition for a given wavelength and look angle. For example, at a look angle of 45 deg, a 25-cm radar will be most sensitive to a surface roughness of approximately 18 cm. Physically, the Bragg condition corresponds to the case where the projected wave vector is equal to half the wave vector of a certain spectral component of the surface. This results in a resonance effect and a strong return.

The term I is related to a double Bragg resonance effect, where the radar wave combinations could result in resonance in this case. This implies that I is related to the overall roughness spectrum and W is related to only one component of that spectrum. For small tilt angles, σ_{HH} is proportional to W to the first order of approximation. This implies that σ_{HH} is also proportional to the spectral component of the surface that satisfies the Bragg condition and σ_{HV} is proportional to the overall roughness spectrum.

5. The Effect of Surface Slope

The effect of surface slope is related to both tilt angle perpendicular to the plane of incidence and to look angle, since a change in look angle is similar to a change in slope in the plane of incidence. For small tilt angles perpendicular to the plane of incidence, A (and σ_{HH}) is proportional to $\cos^2 \delta$, while E (and σ_{HV}) is proportional to $\cos^4 \delta$. This implies that σ_{HV}) is more sensitive to δ than σ_{HH}; σ_{HH} becomes sensitive to surface slope only at θ larger than about 65 deg (see Fig. A-4). The comparison of the behavior of direct and cross-polarized images as a function of look angle cannot be generalized because of the strong dependence on W and I.

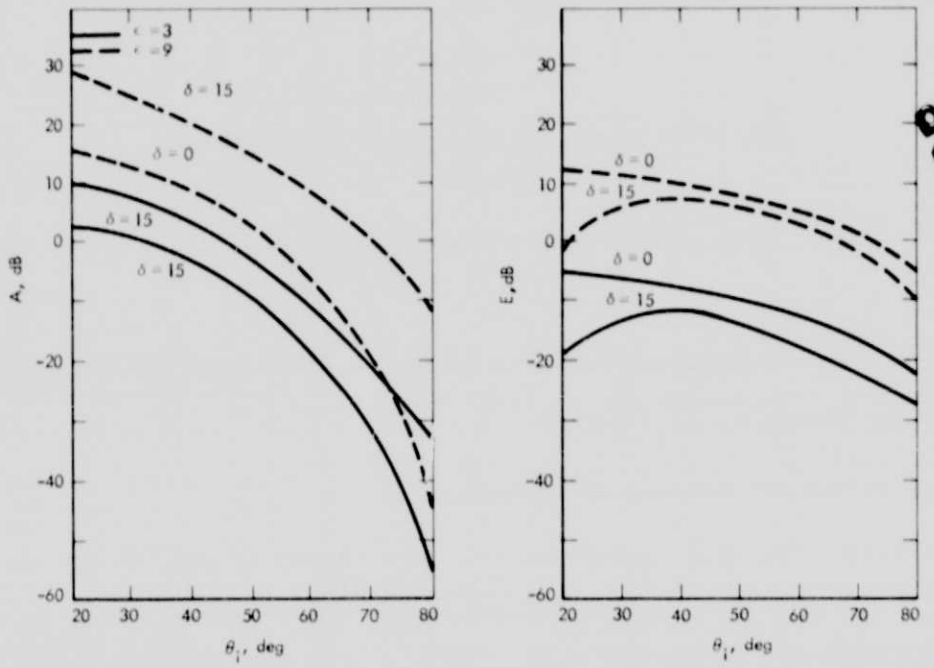

Fig. A-4. Behavior of terms A (HH) and E (HV) in backsactter equation (δ = tilt angle perpendicular to incident beam, ε = dielectric constant, θ_i = incidence angle; from Daily et al., 1978)

6. The Effect of Dielectric Constant

The dielectric constant increases almost linearly with increasing moisture content. The backscatter in both HH and HV images increases with increasing dielectric constant because the reflectivity is higher for larger dielectric constant discontinuities at the reflecting surface. In the case of large dielectric constant and $\delta = 0$, σ_{HH} is independent of and σ_{HV} is proportional to dielectric constant.